

transform infrared (FTIR) spectrometer, corresponding to a linewidth of ~ 3 GHz at a current of 1.4 mA and a detected power of ~ 7 pW. As the current is increased beyond this value, any further narrowing of the transition is hidden behind the limitation of our measurement system. The plot of the linewidth versus injected current combined with the super-exponential increase of the optical power in Fig. 2A strongly suggests that the device is reaching the laser threshold regime near to 1.5 mA. However, the gain in our structure is not sufficient to operate the device clearly in the regime above the lasing threshold.

To access the operation in this regime, we have enhanced the gain of the active medium by immersing the device in a strong magnetic field perpendicular to the quantum wells plane. The magnetic field breaks the in-plane parabolic energy dispersion of the electronic subbands and leads to the formation of discrete Landau levels, allowing the creation of quasi-zero-dimensional states. The spacing of the Landau levels is equal to the cyclotron energy $E_c = \hbar e B / m^*$, where \hbar is Planck's constant divided by 2π , B is the magnetic field, e is the electron charge, and m^* is the effective mass of the electron. By varying the relative ratio between the cyclotron energy and sub-band energy spacing, the electron dynamics and the subsequent lasing properties of a terahertz quantum cascade laser are strongly affected (31). The optical characteristics of the LC laser in a magnetic field of 2.3 T (Fig. 2C) show that, above the threshold, the power increases linearly with the current up to 16 nW until the electrical roll-over is reached. The onset of lasing is accompanied by an abrupt decrease of the differential resistance and is a clear demonstration of the lasing threshold (32). By measuring the threshold current of a control laser with a conventional metal-metal waveguide, we estimate an enhancement of the gain due to the magnetic field by 5 to 10% at 2.3 T.

A number of resonant cavities have been fabricated, continuously modifying the value of the inductor. As expected, the emission spectra (Fig. 3) shift correspondingly between 1.43 and 1.57 THz. The spectra of the devices operating in the edge of the gain curve are barely reaching the threshold regime because they are strongly detuned from the maximum of the gain curve.

Our ultrasmall, electrically injected laser based on a resonator combines elements from microwave electronics with a gain medium. The strong confinement achievable with resonant LC cavities is of great interest for both applications and quantum optics studies. Our results can be seen as implementing gain in one cell of a LC-based metamaterial (33). Because of its monomode output, low dissipation, and tunability, such a source could be integrated with hot-electron bolometers to create arrays of highly sensitive heterodyne receptors for demanding applications such as radio-astronomy (34). The strong coupling that is achieved in such resonators could also lead to interesting applications, not only for optical sources, but also

for detectors and modulators, as the latter devices do not require very high Q factors and would benefit greatly from the reduction of the mode volume brought by this resonator. V_{eff} can be reduced almost at will, as long as the reduction in the capacitance can be compensated by an increase of the inductance to keep the product constant. An attractive feature of the LC resonator is the spatial separation of the electric and magnetic fields, simultaneously allowing extremely high confinement of the electric field and an efficient out-coupling to the environment by the magnetic field. An LC resonator with a bent inductor could act as a magnetic loop antenna, which is efficiently coupled to both the vacuum and the matter, such as a quantum dot (SOM text S3). The design concept of the LC resonator can be extended from the terahertz range to near-infrared frequencies (SOM text S4).

References and Notes

1. E. M. Purcell, *Phys. Rev.* **69**, 681 (1946).
2. J. Gérard *et al.*, *Phys. Rev. Lett.* **81**, 1110 (1998).
3. S. Ogawa, M. Imada, S. Yoshimoto, M. Okano, S. Noda, *Science* **305**, 227 (2004); published online 3 June 2004 (10.1126/science.1097968).
4. C. Weisbuch, M. Nishioka, A. Ishikawa, Y. Arakawa, *Phys. Rev. Lett.* **69**, 3314 (1992).
5. K. J. Vahala, *Nature* **424**, 839 (2003).
6. F. Koyama, *Lightwave Technol.* **24**, 4502 (2006).
7. R. Coccioli, M. Boroditsky, K. W. Kim, Y. Rahmat-Samii, E. Yablonovitch, *IEE Proc. Optoelectron.* **145**, 391 (1998).
8. O. Painter *et al.*, *Science* **284**, 1819 (1999).
9. H.-G. Park *et al.*, *Science* **305**, 1444 (2004).
10. J. Scheuer, W. Green, G. DeRose, A. Yariv, *Appl. Phys. Lett.* **86**, 251101 (2005).
11. K. Nozaki, T. Baba, *Appl. Phys. Lett.* **88**, 211101 (2006).
12. M. Hill *et al.*, *Nat. Photonics* **1**, 589 (2007).
13. R. F. Oulton *et al.*, *Nature* **461**, 629 (2009).

14. S. Kühn, U. Håkanson, L. Rogobete, V. Sandoghdar, *Phys. Rev. Lett.* **97**, 017402 (2006).
15. M. A. Noginov *et al.*, *Nature* **460**, 1110 (2009).
16. J. Slater, *Rev. Mod. Phys.* **18**, 441 (1946).
17. The lumped element circuit approach was proposed at optical frequencies (18).
18. N. Engheta, *Science* **317**, 1698 (2007).
19. T. J. Yen *et al.*, *Science* **303**, 1494 (2004).
20. S. Linden *et al.*, *Science* **306**, 1351 (2004).
21. J. Faist *et al.*, *Science* **264**, 553 (1994).
22. R. Köhler *et al.*, *Nature* **417**, 156 (2002).
23. Y. Chassagneux *et al.*, *Appl. Phys. Lett.* **90**, 091113 (2007).
24. H. Wheeler, *IRE Trans. Antennas Propag.* **35**, 1479 (1947).
25. A. Wallraff *et al.*, *Nature* **431**, 162 (2004).
26. C. Walther *et al.*, *Appl. Phys. Lett.* **91**, 131122 (2007).
27. B. Williams, S. Kumar, Q. Hu, J. Reno, *Opt. Express* **13**, 3331 (2005).
28. Multiphysics Modeling and Simulation Software (COMSOL) was used for our simulations (www.comsol.com).
29. M. Ordal, R. Bell, R. Alexander Jr., L. Long, M. Querry, *Appl. Opt.* **26**, 744 (1987).
30. G. Scalari *et al.*, *Laser and Photonics Rev.* **3**, 45 (2009).
31. G. Scalari *et al.*, *Phys. Rev. Lett.* **93**, 237403 (2004).
32. C. Sirtori *et al.*, *IEEE J. Quantum Electron.* **34**, 1722 (1998).
33. M. Wegener *et al.*, *Opt. Express* **16**, 19785 (2008).
34. J. Gao *et al.*, *Appl. Phys. Lett.* **86**, 244104 (2005).
35. We thank the Swiss National Science Foundation and the National Center of Competence in Research "Quantum Photonics" for support and L. Nevou for key contributions to the reflectivity measurement. This work was partly carried out in the Center for Micro- and Nanotechnology (FIRST) at ETH Zurich. J.F. would like to acknowledge fruitful discussions with E. Yablonovitch and A. Imamoglu.

Supporting Online Material

www.sciencemag.org/cgi/content/full/327/5972/1495/DC1

Materials and Methods

SOM Text

Figs. S1 to S4

References

12 October 2009; accepted 11 January 2010

10.1126/science.1183167

The Climatic Signature of Incised River Meanders

Colin P. Stark,^{1*} Jonathan R. Barbour,¹ Yuichi S. Hayakawa,² Tsuyoshi Hattajji,³ Niels Hovius,⁴ Hongey Chen,⁵ Ching-Wee Lin,⁶ Ming-Jame Horng,⁷ Kai-Qin Xu,^{8,9} Yukitoshi Fukahata¹⁰

Climate controls landscape evolution, but quantitative signatures of climatic drivers have yet to be found in topography on a broad scale. Here we describe how a topographic signature of typhoon rainfall is recorded in the meandering of incising mountain rivers in the western North Pacific. Spatially averaged river sinuosity generated from digital elevation data peaks in the typhoon-dominated subtropics, where extreme rainfall and flood events are common, and decreases toward the equatorial tropics and mid-latitudes, where such extremes are rare. Once climatic trends are removed, the primary control on sinuosity is rock weakness. Our results indicate that the weakness of bedrock channel walls and their weakening by heavy rainfall together modulate rates of meander propagation and sinuosity development in incising rivers.

In humid, rapidly eroding (*I*) montane environments such as the Cascades (2), Japan (3), and Taiwan (4), lateral erosion along the banks and walls of bedrock-floored river channels (5–13) can be as important a process as vertical incision. Rates of lateral erosion can exceed down-cutting rates by over 10 times as a bedrock channel widens (11, 12) or meanders (5–10, 13, 14). With time, such horizontal cutting is known to

generate sinuous channels (5–10, 13–20), very broad channels (8, 9), bedrock-floored cut (strath) terraces (2, 5, 6, 13, 21), asymmetric valleys (7, 17–19), and even meander cut-off loops (8–10, 13, 15–20). In particular, field observations (8–10) and theoretical considerations (22, 23) indicate that the majority of the meanders and high sinuosities seen in such bedrock rivers are actively generated by erosive lateral chan-

nel motion (5–9), although there are certainly cases in which meandering forms are inherited (15) as channels maintain their sinuous shape during down-cutting (19, 20).

Three key factors determine the rate of lateral channel erosion: (i) flood shear (5, 6, 10–12) and particle momentum flux (24) on the channel walls, which induce bedrock wear (12, 14, 25, 26) and remove debris dumped from adjacent hill slopes; (ii) bedrock weakness (5, 6, 9, 25, 26), which sets both the basic rate of flow-driven wear (25) and the instability of channel bedrock walls and hill slopes (27); and (iii) rainfall intensity and duration, which modulate bedrock instability and adjust the rate of wall erosion by rock falls and landslides (27). Transient alluvial cover of the

bedrock bed is also important, but only in the relative sense (14, 21) of reducing down-cutting rates while leaving wall erosion rates unaffected.

These observations led us to pose two hypotheses: (i) The degree of sinuosity development in a network of bedrock rivers may provide a quantifiable measure of the rate of lateral channel erosion; and (ii) catchment-scale averaged sinuosity in humid mountain rivers should correlate on a regional scale both with rock type and with rainfall and flood frequency and magnitude. Underpinning these hypotheses is the observation (19) (fig. S2) that a range of phenomena—fluxes of debris from adjoining hill slopes, differential erosion into heterogeneous bedrock, big shifts in formative discharge through stream capture, catchment growth or shrinkage, and climate change, not to mention necking and loop cut-off—act to disrupt meander growth and ultimately limit the development of sinuosity. Over time, competition between lateral channel erosion and meander-limiting processes yields a spread of reach sinuosities across a catchment whose average is expected to depend on bedrock erodibility and climatic conditions.

Previous support for the two hypotheses comes from studies of laterally mobile bedrock rivers in Japan (5–7), where flood shear and rock strength were found to correlate well with horizontal erosion and lateral channel migration during 30,000 years of vertical incision. However, no studies of sinuosity have been attempted at a scale large enough to identify climatic trends,

chiefly because the necessary data have not been available in consistent digital form at a regional scale. With the recent availability of 3-arc sec Shuttle Radar Topography Mission (SRTM) digital elevation model data for much of the globe, as well as digital geology maps and archives of meteorological and hydrologic data, this impediment no longer exists.

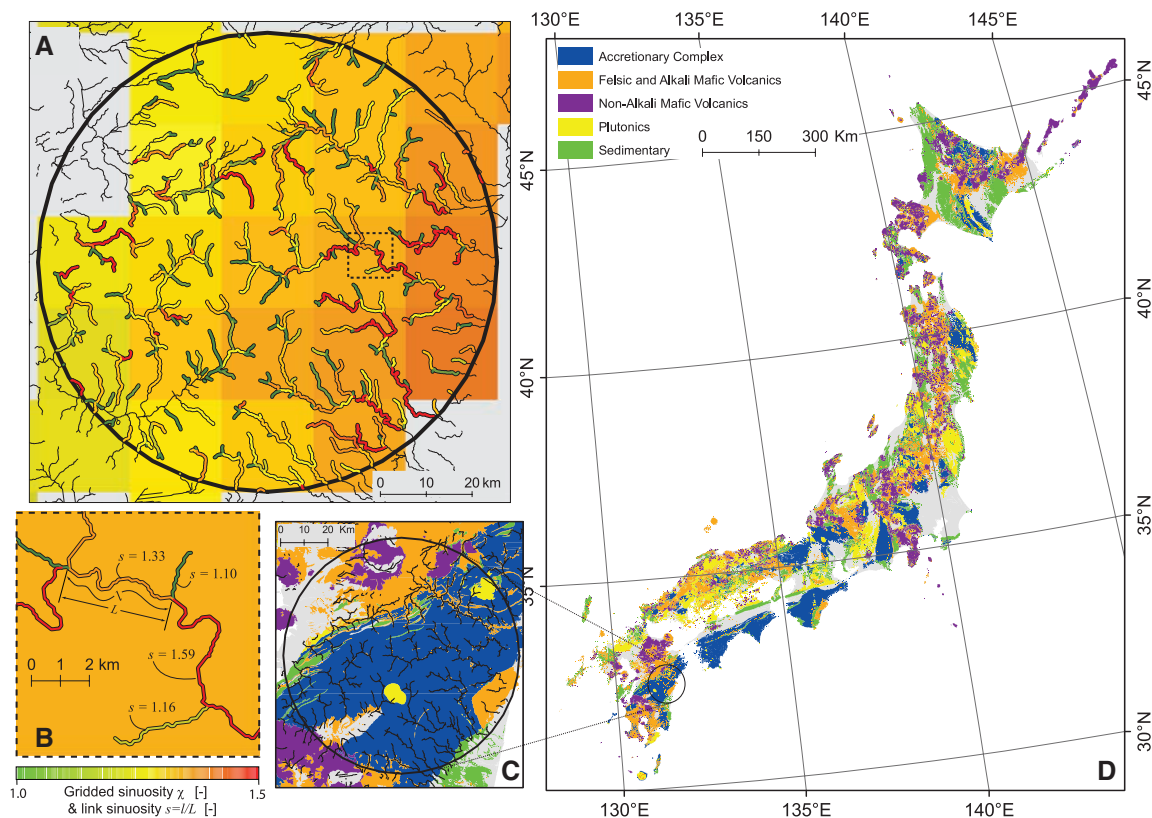
To test the two hypotheses, we quantified upland river sinuosity (Fig. 1, A and B) in the western North Pacific using SRTM data. We initially focused on Japan because of its broad dynamic range of storm rainfall. We processed a seamless, high-resolution, vector geology map of Japan (3) (Fig. 1, C and D) to identify incising bedrock channels, segment them into reaches between stream junctions, and group them into five broad lithological classes (28) that span areas sufficient for statistical analysis. Channel-reach sinuosities s for each of the five classes were then aggregated within 100-km moving windows and converted into gridded maps of regionalized average sinuosity χ (28).

Next, we correlated χ with daily rainfall statistics, generated from 20- to 30-year records from a dense network of 1666 stations (Fig. 2A) across the archipelago (28), to assess the dual influences of lithology and climate on sinuosity on a subregional scale. Scaling up to the western North Pacific, we generated a single grid of sinuosity χ for a group of lithologies chosen from the Japan analysis for their similar apparent erodibility (Fig. 2B). Finally, we correlated the sinuosity

¹Lamont-Doherty Earth Observatory of Columbia University, Palisades, New York 10964, USA. ²Center for Spatial Information Science, University of Tokyo, 5-1-5 Kashiwanoha, Kashiwa, Chiba 277-8568, Japan. ³Graduate School of Life and Environmental Sciences, University of Tsukuba, Ibaraki 305-8572, Japan. ⁴Department of Earth Sciences, University of Cambridge, Downing Street, Cambridge CB2 3EQ, UK. ⁵Department of Geosciences, National Taiwan University, No. 1, Sec. 4, Roosevelt Road, Taipei 10617, Taiwan. ⁶Department of Earth Sciences, National Cheng Kung University, Tainan, Taiwan. ⁷Water Resources Agency, Ministry of Economic Affairs, Hsin-Yi Road, Taipei, Taiwan. ⁸National Institute for Environmental Studies, 16-2 Onogawa, Tsukuba 305-8506, Japan. ⁹State Key Laboratory of Water Resources and Hydropower Engineering Science, Wuhan University, Wuhan 430072, China. ¹⁰Disaster Prevention Research Institute, Kyoto University, Gokasyo, Uji, Kyoto 611-0011, Japan.

*To whom correspondence should be addressed. E-mail: cstark@ldeo.columbia.edu

Fig. 1. (A) Drainage delineation and sinuosity calculation. (B) A zoom shows how each reach sinuosity $s = l/L$ is the ratio of along-stream l to the distance the crow flies L between channel junctions. Regionalized sinuosity χ is the weighted sum (28) of the link sinuosities within the 100-km-diameter circle in (A) and (C); χ is gridded at a resolution of 20 km. (D) Simplified bedrock geology of Japan based on a 1:200,000 synthesis carried out by the Geological Survey of Japan. Large contiguous areas of Quaternary sediments are indicated in gray, as are metamorphic rocks, which represent a very small fraction of total bedrock exposure; both are excluded from sinuosity analysis. Regionalized sinuosity χ was mapped by delineating reach sinuosities on each lithology mask separately.



grid with typhoon-track (Fig. 3), stream-gauge, and rain-gauge data (Fig. 4) around the western Pacific Rim (28).

In the Japan analysis, spatial correlation of the sinuosity χ grid with station rainfall statistics [such as frequency of rainfall exceedance F_{rx} of

50 mm/day (28)] revealed approximately linear trends (table S1) for almost all rock types (Fig. 2A), with sinuosity χ rising with increasing “storminess” from north to south. To isolate the dependence on rock type (Fig. 2), values of χ were projected from a common origin onto a reference

$F_{rx} = 10 \text{ year}^{-1}$, and a probability density function (PDF) $p(\chi)$ was generated for each lithology class.

The PDFs show (Fig. 2B) that the most sinuous incising rivers are found in accretionary complex lithologies (8, 9). These rocks are predominantly low-strength, highly erodible (6, 8, 9), silt and fine-sand turbidites with intermittent coarser, stronger units; channels cut into these rocks are known for their high degree of meandering (8, 9). The least sinuous incising rivers are found in generally erosion-resistant (5), non-alkali mafic volcanics, which include rocks ranging in strength from very strong, fresh basaltic lavas to weathered, unwelded, much weaker tuffs (5). The greatest regional variation in sinuosity χ and its strongest correlation with F_{rx} are seen in the weak accretionary complex rocks, whereas the strong, nonalkali mafic volcanics show the least variation in χ and its weakest correlation with F_{rx} (Fig. 2A and table S1).

When combined with past studies of erosion rates and fractured rock strength in Japan (5, 6), our results (Fig. 2 and table S1) indicate that rock erodibility (5, 6, 9, 25) is the primary control on sinuosity development and incised meandering (8, 9). Heavy rainfall frequency or storminess exerts a clear secondary control on sinuosity development, particularly in weaker rock types.

Next we examined sinuosity correlations on a subhemispheric scale. By combining the high-resolution geology data in Japan with low-resolution digital geology for the western North

Fig. 2. (A) Sinuosity χ versus storminess expressed as the frequency F_{rx} at which rainfall accumulation exceeds 50 mm in 24 hours; (B) PDFs of detrended sinuosity $p(\chi|F_{rx} = 10)$, generated by projecting each value of $\chi(F_{rx})$ onto $\chi(10)$ along lines with a common origin at $\chi = 1.16$ (the estimated average for all the data combined). Blue diamonds, accretionary complex; green squares, nonaccretionary complex sedimentary rock; yellow triangles, plutonics; orange triangles, felsic and alkali mafic volcanics; purple circles, nonalkali mafic volcanics; dashed lines, linear regressions. Error bars are 1σ SDs.

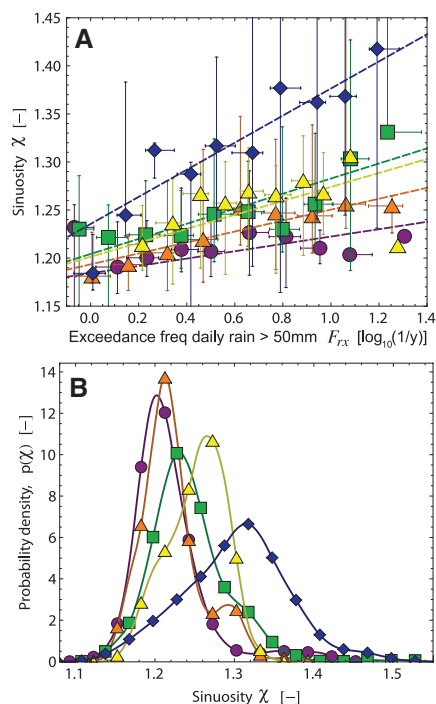
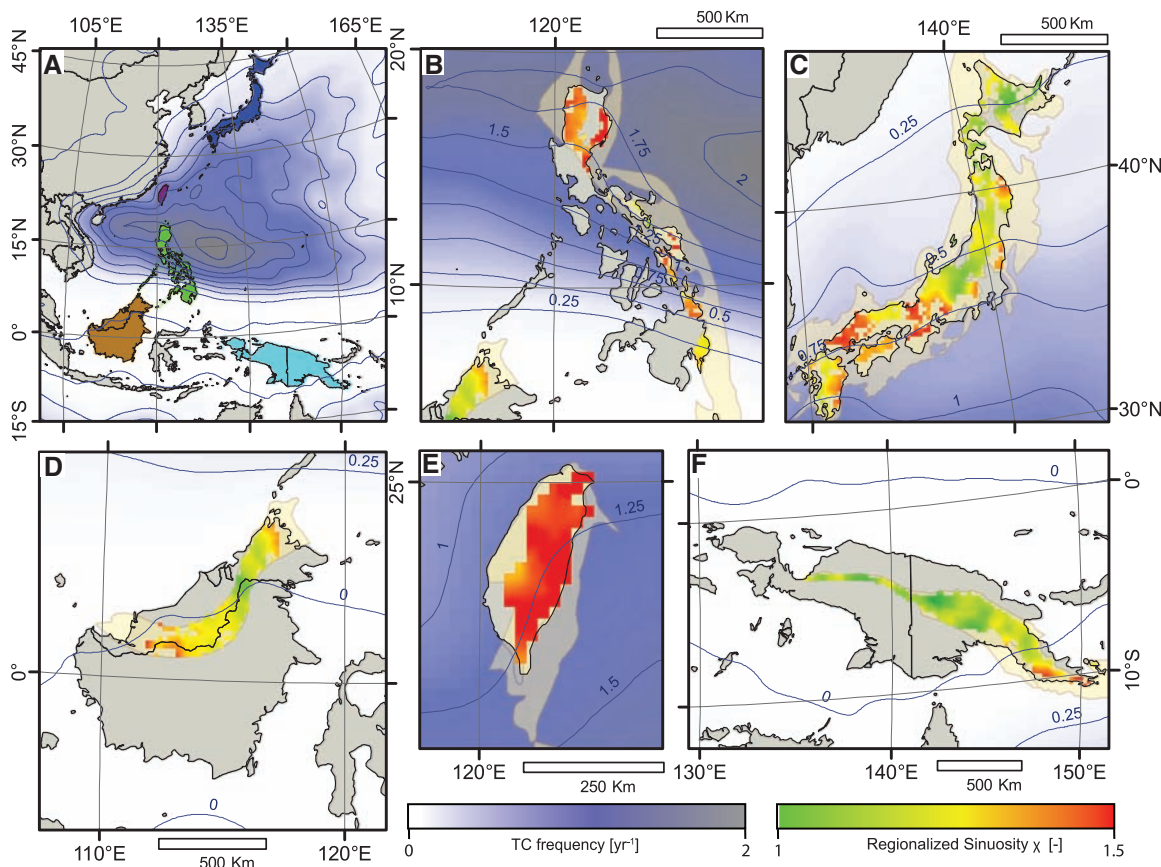


Fig. 3. (A) Regionalized sinuosity χ (green/yellow/red for range 1 to 1.5) and typhoon strike frequency (blue contour intervals of 0.25 per year) across the western North Pacific. The studied islands are shown as follows: (B) the Philippines (green), (C) Japan (dark blue), (D) Borneo (brown), (E) Taiwan (purple), and (F) New Guinea (cyan). Analysis is restricted to high-relief areas on subduction complex lithologies chosen from the Japan analysis for similarity in their apparent erodibility; masked-out regions are shown in gray.



Pacific, we were able to restrict χ mapping to a subset of lithologies (mafic and nonmafic volcanics, plutonics, and sedimentary rocks) with broadly similar sensitivity of sinuosity to storm frequency F_{rx} (Fig. 2). We excluded geological formations dissimilar to those found in Japan (such as those in southern Borneo), whose sinuosity sensitivity was not calibrated by the Japan analysis. The resulting clipping mask for this geological assemblage was used to prune the stream networks and generate another map of sinuosity χ spanning an area from the equatorial tropics to the mid-latitudes (Fig. 3).

We correlated (Fig. 4) the regional sinuosity χ grid with records of monthly mean rainfall, daily river discharge data, and a spatial PDF of typhoon strike frequency (Fig. 3) generated from tropical cyclone track records (28). We found roughly linear trends in sinuosity with both rainfall variability, expressed as the coefficient of variation R_{cv} [Fig. 4A; Kendall's rank correlation coefficient (τ_k) = 0.44, Pearson's correlation coefficient (r^2) = 0.40], and with relative flood intensity, expressed as the 99th percentile discharge normalized by catchment area Q_{99}/A (Fig. 4B; τ_k = 0.48, r^2 = 0.42). Sinuosity is highest in the monsoonal, typhoon-prone northern Philippines, southern Japan, and Taiwan, where heavy rainfall frequency and flood intensity are highest

(1, 3, 4, 29). Low-sinuosity rivers are more commonly found in mid-latitude northern Japan and in the equatorial tropics, where extremely heavy storms are far less frequent and flood variability is much lower. This regional dependence on storm climatology is confirmed by the correlation seen between sinuosity and typhoon strike frequency (Fig. 4C; τ_k = 0.50, r^2 = 0.45) and is corroborated by the peaked relationship seen between sinuosity and latitude (Fig. 4D).

Our combined results show that once account is taken of rock type, sinuosity records a measurable signature of storminess—a key factor in climate-landscape dynamics (30). Conversely, our observations show that if the modulating effect of storminess is removed, sinuosity provides a proxy measure for bedrock erodibility.

This dependence of sinuosity χ on bedrock erodibility (Fig. 2), as well as the ubiquitous association of incised meanders with weak bedrock (5, 6, 8–10, 13, 20), indicates that horizontal channel erosion rates are much more sensitive to greater rock erodibility than are vertical channel erosion rates. This asymmetry lies in the dual control of lateral channel motion by both flow-driven wear of the channel wall (12, 24, 26) and mass-wasting erosion of the adjoining hill slope, versus the single control on vertical incision by flow-driven wear of the bed alone (14, 25). Bed

sediment cover augments the asymmetry (14) but is not its cause.

The climatic signature expressed in sinuosity comes from an amplification of this asymmetric sensitivity. More frequent heavy rainfall means that channel walls and adjoining hill slopes are destabilized more often and are more prone to lateral erosion (27); it also means an increase in flood frequency, flow shear, and sediment momentum flux on both channel walls and beds. The combined effect is to raise wall erosion rates more than bed erosion rates and to accelerate sinuosity development (fig. S2). In the western North Pacific, this phenomenon ultimately leads to a correlation between typhoon strike frequency and incised channel sinuosity.

The strength of the observed climatic signature underlines the strong coupling between climate and erosion in these island mountain landscapes (1, 4, 29, 30) and the extent to which their morphology reflects recent [late Pleistocene to present (5, 6, 13)] climatic conditions. This coupling is much weaker where erosion rates are much lower, and therefore sinuosity development in such environments [such as the Colorado Plateau (20)] will reflect a much longer-term integration of weather patterns.

Even for the western North Pacific there is significant disparity between the brief time span of available meteorological and hydrologic data [~20 to 60 years (28)] versus the time scale over which bedrock meanders have evolved [~1000 to ~100,000 years (5, 6, 13)]. We nevertheless have confidence that our correlations with storminess have meaning, because the regional pattern of storminess is so strongly tied to the average distribution of typhoon tracks (Figs. 3 and 4). The shape of this distribution is determined by the location of tropical cyclogenesis (currently between 8°N and 25°N in the western North Pacific) and by the steering effect of the large-scale circulation of the atmosphere (31). Both undoubtedly change on interannual to multimillennial time scales, but it is reasonable to infer that the broad latitudinal trend in typhoon strikes, with its peak in the subtropics (Fig. 4D), has remained roughly constant since the current plate-tectonic configuration of the western North Pacific was established several million years ago.

The studied landscapes and their high sediment fluxes also exhibit a strong coupling with tectonics (1, 4, 30), but our results suggest that rock uplift rate is a much less plausible explanatory variable for sinuosity χ than climate. Sinuosities are highest in the northern Philippines (Luzon; Figs. 3 and 4) and second highest in Taiwan, which is consistent with our observation that typhoon strike frequencies and storminess measures are highest in Luzon and second highest in Taiwan, but is inconsistent with the relatively low late Pleistocene–Holocene uplift rates seen in Luzon (~1 mm/year) (32) as compared with those in Taiwan [~6 mm/year (4, 30, 33)]. Similarly, the north-south trend in increasing sinuosity seen in Japan (Fig. 2A) is not expressed in the regional

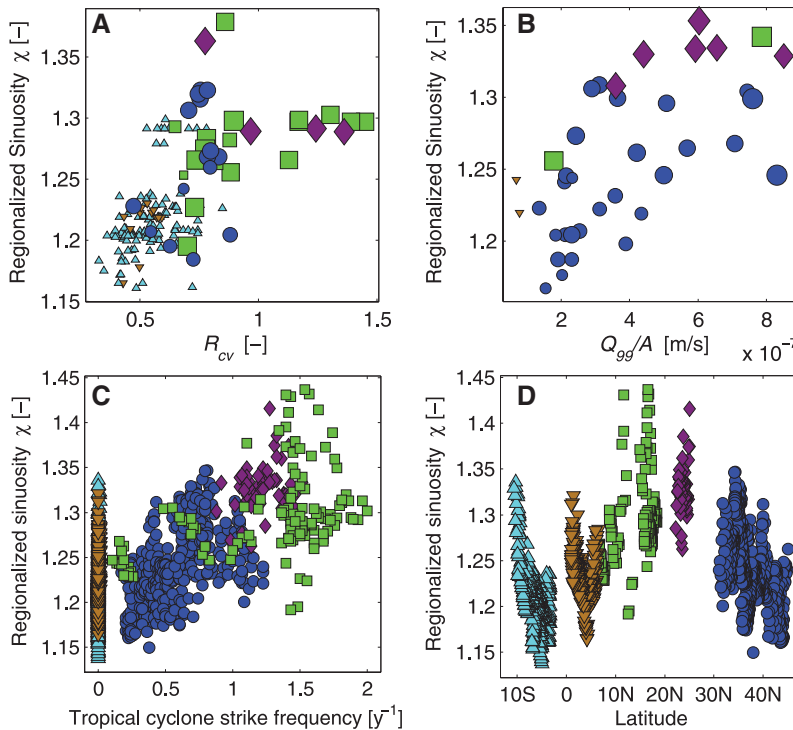


Fig. 4. Regional correlation analyses of sinuosity χ . Colors and symbols are as follows: dark blue circles, Japan; purple diamonds, Taiwan; green squares, the Philippines; brown downward triangles, Borneo; cyan upward triangles, New Guinea. (A) With coefficient of variation $R_{cv} = R_{\sigma}/R_{\mu}$ (where σ is standard deviation and μ is the mean) of monthly rainfall at 169 rain gauges across the western North Pacific (τ_k = 0.44, r^2 = 0.40). Symbol sizes correspond to typhoon strike frequency. (B) With relative flood intensity Q_{99}/A (99th percentile discharge normalized by catchment area A) measured at 38 river gauges across the western North Pacific (τ_k = 0.48, r^2 = 0.42). (C) With typhoon strike frequency (τ_k = 0.50, r^2 = 0.45; excluding Borneo and New Guinea where typhoons are absent). (D) With latitude, showing a peak in the typhoon-dominated subtropics.

Downloaded from www.sciencemag.org on March 24, 2010

pattern of uplift rates inferred from marine isotope stage 5.5 marine terrace elevations (33). If uplift rate does play a role, it may be in modulating channel steepness as a function of sinuosity (fig. S3).

References and Notes

- J. D. Milliman, J. P. M. Syvitski, *J. Geol.* **100**, 525 (1992).
- F. J. Pazzaglia, M. T. Brandon, *Am. J. Sci.* **301**, 385 (2001).
- Y. S. Hayakawa, T. Oguchi, *Geomorphology* **111**, 27 (2009).
- S. J. Dadson *et al.*, *Nature* **426**, 648 (2003).
- T. Suzuki, *Trans. Jpn. Geomorphol. Union* **3-1**, 1 (1982).
- T. Suzuki, *Trans. Jpn. Geomorphol. Union* **4-1**, 33 (1983).
- M. Hirano, *Trans. Jpn. Geomorphol. Union* **1-2**, 117 (1981).
- R. Yagi, H. Ikeda, *Bull. Environ. Res. Center Univ. Tsukuba* **22**, 1 (1997).
- A. Nakano, H. Ikeda, *Bull. Environ. Res. Center Univ. Tsukuba* **24**, 1 (1999).
- J. R. Barbour *et al.*, *Geophys. Res. Lett.* **36**, L04401 (2009).
- C. P. Stark, *Geophys. Res. Lett.* **33**, L04402 (2006).
- J. M. Turowski, D. Lague, N. Hovius, *J. Geophys. Res.* **114** (F3), F03016 (2009).
- J. B. H. Shyu, K. Sieh, J.-P. Avouac, W.-S. Chen, Y.-G. Chen, *J. Geophys. Res.* **111** (B8), B08403 (2006).
- J. M. Turowski, D. Lague, N. Hovius, *J. Geophys. Res.* **112**, (F4), F04006 (2007).
- W. M. Davis, *Science* **21**, 225 (1893).
- A. Winslow, *Science* **22**, 31 (1893).
- R. H. Mahard, *J. Geomorphol.* **5**, 32 (1942).
- H. Blank, *Geol. Soc. Am. Bull.* **81**, 3135 (1970).
- G. H. Dury, *Am. J. Sci.* **252**, 193 (1954).
- D. R. Harden, *Geol. Soc. Am. Bull.* **102**, 233 (1990).
- G. S. Hancock, R. S. Anderson, *Geol. Soc. Am. Bull.* **114**, 1131 (2002).
- S. Ikeda, G. Parker, K. Sawai, *J. Fluid Mech.* **112**, 363 (1981).
- G. Seminara, *J. Fluid Mech.* **554**, 271 (2006).
- J. G. A. Bitter, *Wear* **6**, 169 (1963).
- L. S. Sklar, W. E. Dietrich, *Geology* **29**, 1087 (2001).
- K. Hartshorn, N. Hovius, W. B. Dade, R. L. Slingerland, *Science* **297**, 2036 (2002).
- F. Guzzetti, S. Peruccacci, M. Rossi, C. P. Stark, *Meteorol. Atmos. Phys.* **98**, 239 (2007).
- See supporting material on Science Online.
- J. Galewsky *et al.*, *J. Geophys. Res.* **111** (F3), F03014 (2006).
- S. D. Willett *et al.*, Eds., *GSA Spec. Pap.* **398**, Penrose Conf. Ser. (2006).
- J. C. L. Chan, *Annu. Rev. Fluid Mech.* **37**, 99 (2005).
- Y. Maeda *et al.*, *Quat. Int.* **115–116**, 15 (2004).
- Y. Ota, M. Yamaguchi, *Quat. Int.* **120**, 105 (2004).
- This study was supported by NASA, NSF (Earth Sciences Division, Geomorphology and Land-use Dynamics Program), and the Taiwan National Science Council. We thank W. E. Dietrich, G. Parker, and E. E. Wohl for enlightening discussions and C.-H. Jen, C. Huang, T.-C. Yi, and M. Tajikara for help in the field.

Supporting Online Material

www.sciencemag.org/cgi/content/full/327/5972/1497/DC1

Methods

Figs. S1 to S3

Table S1

9 November 2009; accepted 5 February 2010

10.1126/science.1184406

Transition-State Spectroscopy of Partial Wave Resonances in the F + HD Reaction

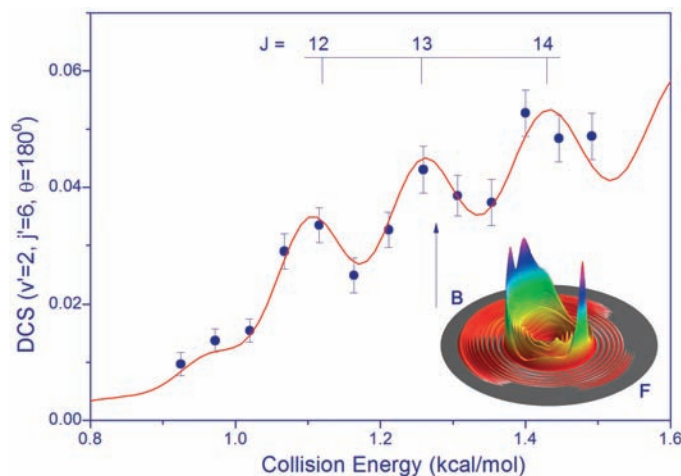
Wenrui Dong,* Chunlei Xiao,* Tao Wang, Dongxu Dai, Xueming Yang,† Dong H. Zhang†

Partial wave resonances, quasi-bound resonance states with well-defined rotation in the transition state region of a chemical reaction, play a governing role in reaction dynamics but have eluded direct experimental characterization. Here, we report the observation of individual partial wave resolved resonances in the $F + HD \rightarrow HF + D$ reaction by measuring the collision energy-dependent, angle- and state-resolved differential cross section with extremely high resolution, providing a spectroscopic probe to the transition state of $F + HD \rightarrow HF + D$. The agreement of the data with the high-level theoretical calculations confirms the sensitivity of this probe to the subtle quantum mechanical factors guiding this benchmark reaction.

Direct characterization of transition states, the fleeting structures at the boundary between the reactants and products in molecular transformations, is one of the grand challenges in physical chemistry (1–3). Substantial progress toward this goal has been made in the past two decades by using negative-ion photodetachment spectroscopy, which probes a reaction transition state by directly photodetaching an electron from an appropriate negative-ion precursor that has a similar geometric structure to the transition state (4). However, it is much more difficult to measure the transition-state structures in crossed molecular-beam experiments, even with full quantum mechanical state resolution of the initial and final states, because in most chemical reactions experimental observables come from the contributions of collisions with many partial waves, or in classical terms, of collisions with a range of impact parameters or total angular momentum. A partial wave is a quantum-scattering

state with a well-defined total angular momentum quantum number (J), which specifies the overall rotation of the reaction system and is conserved in the reaction process. A full reaction

Fig. 1. Experimental and theoretical DCS of the $HF(v' = 2, j' = 6)$ product of the $F(^2P_{3/2}) + HD(j = 0)$ reaction in the backward scattering direction. The solid circles are experimental data; the red curve, the result of full quantum dynamics calculations convoluted with the experimental resolution and shifted 0.03 kcal/mol lower in energy. The error bars in the experimental data are the estimated measurement errors ($\pm 1\sigma$) for the $HF(v' = 2, j' = 6)$ product peak intensity (fig. S1) in the collision energy scan. The three peaks are assigned to the partial wave Feshbach resonances of $J = 12, 13$, and 14 in the $F + HD \rightarrow HF + D$ reaction, as explained in the text. The three-dimensional DCS shown was measured at 1.285 kcal/mol, with F and B indicating the forward- and backward-scattering, respectively, directions for HF with respect to the F-atom beam direction.



State Key Laboratory of Molecular Reaction Dynamics, Dalian Institute of Chemical Physics, Chinese Academy of Sciences, Dalian 116023, Liaoning, People's Republic of China.

*These authors contributed equally to this work.

†To whom correspondence should be addressed. E-mail: xmyang@dicp.ac.cn (X.Y.); zhangdh@dicp.ac.cn (D.H.Z.)